[AMERICAN JOURNAL OF SCIENCE, VOL. 287, DECEMBER, 1987, P. 1008–1040]

GEOCHEMICAL SELF-ORGANIZATION II: THE REACTIVE-INFILTRATION INSTABILITY†

PETER ORTOLEVA*, JOHN CHADAM*, ENRIQUE MERINO*, AND A. SEN**

*Geo-Chem Research Associates, 400 East Third Street, Bloomington, Indiana 47401

ABSTRACT. Aqueous solutions that flow through a porous rock and react with its mineral components establish a moving reaction front in the rock. As it advances, the front can become regularly scalloped through the action of the reactive infiltration instability: where the porosity is larger than elsewhere in the rock, the local water flux is greater, mineral grains dissolve faster, the permeability also increases faster, and the front accelerates. The increase in local flux comes about by capture of flux from nearby points; in these, the front decelerates.

The phenomenon can be represented by a system of differential equations of mass conservation that account for coupled reaction, diffusion, and infiltration. The change in water flow velocity is linked through the permeability to the porosity changes brought about by mineral dissolution. The local, instantaneous rate of mineral dissolution in turn depends on the rate of supply of ions by transport. The scaling of the equations and the introduction into them of a fundamental, very small natural parameter (namely, the ratio of typical aqueous concentrations to mineral densities, which can range from 10^{-3} to 10^{-9} or less at temperatures <250°), facilitate reducing the system of equations to a "free boundary" problem, in which the reaction front is at once a boundary and an unknown. The equations yield the front velocity and width and the temporal *and* spatial distributions of porosity, pore-fluid composition, and fluid pressure.

A linear stability analysis of the set of equations shows that a planar dissolution front is unstable, and that the moving, reactive aqueous solution tends to dissolve out and funnel itself through high-permeability "fingers" through the rock. The analysis predicts the spacing between adjacent fingers. Depending on grain sizes, initial modal amount of reactive mineral in the rock, initial porosity, and composition and velocity of the inlet fluid, the predicted spacing between fingers can range from centimeters to several kilometers. Numerical solution of the nonlinear differential equations in two dimensions also shows that the reaction front can be unstable to formation of fingers.

It is important to note that this analysis demonstrates that such patterns can form in the absence of externally imposed or pre-existing periodicities. They arise spontaneously from the nonlinear feedback mechanism and as such are, by definition, examples of geochemical self-organization.

† Research supported by the U. S. Department of Energy, Basic Energy Sciences, Engineering Research Program, Contract #DE-AC02-82ER12074.

* Indiana University, Bloomington, Indiana 47405

**Department of Mathematics Indiana University-Purdue University, Indianapolis, Indiana 47401

Scalloped fronts observed in clastic rocks, in uranium roll-front deposits, in tropical weathering profiles, in karst rocks, and in skarns are probable evidence of the reactive-infiltration instability.

TABLE 1

Symbols

A	mineral species A; also (in app. A) its concentration in the rock, in moles of A per cm^3 of bulk rock
A_0	value of A in the unaltered rock
a	A/A_0
D*	ratio of diffusion coefficients defined in (VII.A7)
D_f	effective diffusion coefficient of X in the altered rock
D_0	diffusion coefficient of X in water (cm^2/s)
$D(\phi)$	porosity-dependent effective diffusion coefficient of X in the porous medium, (cm^2/s); see (A.5)
f_i	volume fraction of grains of mineral i referred to total grain volume (but not counting pore space); see (VIII.9)
J, θ	packing and geometric factors in the Fair-Hatch eq, (VIII.8)
$\underline{J}$	local flux of X, in moles of X per sec cm^2 of rock cross section
k	reaction rate constant
L_A, L_B	cube root of A and B grain volumes
L_y	dimension of the porous system in the y direction (=direction normal to top and bottom of the aquifer)
m	wave vector in (VIII.2)
m_c	m for which ω is maximum—that is, scallop perturbations of the planar front of wave vector m_c (and wavelength $2\pi/m_c$) grow the fastest.
m_0	maximum value of m for which perturbations can grow; given by (VIII.4)
$\partial/\partial n$	gradient in the direction normal to dissolution interface $S(\underline{r}, t) = 0$
n_A, n_B	grain number density of A and B (number of grains per cm^3 of bulk rock)
$\underline{p}$	fluid pressure
$\underline{r}$	position
S	a function of position and time that is zero at the reaction front, <0 upflow from the front, and >0 downflow from it; see (VI.4)
t	time
$\underline{u}$	normal velocity of the reaction front
$\underline{v}$	infiltration water velocity, cm/s
v_f	water velocity in the altered zone after A has been dissolved out
$v_{f,c}$	critical water velocity in the altered zone beyond which the planar front goes unstable to scalloping in a system of width L_y. Found by solving $m_0(v_{f,c}) = \pi/L_y$; see (VIII.4), (IX.B3)
z	coordinate along overall water flow direction
x, y	y is normal to the top and bottom of the aquifer and to z; x is normal to y and z
X, Y	aqueous species X, Y; also their concentrations in moles per unit of pore volume
X_M	concentration of X in the inlet water
Y^{eq}	Y saturation concentration in presence of mineral A for process (III.1)
α	ratio of water velocity to diffusion coefficient in the altered zone; see (VII.3)
κ^*	ratio defined in (IX.A7)
$\kappa(\phi)$	permeability (a function of porosity) divided by water viscosity
κ_f	value of $\kappa(\phi)$ for the altered rock (where $\phi = \phi_f$)
Γ	ratio of (porosity) times (permeability) ahead of front to that behind it; see (VI.11)
γ	scaled, dimensionless X or Y concentrations; see (VI.2), (A.9)
δ	ratio of typical solute concentration to solid molar density (for example, X_m/ρ_A)
ζ	front-fixed coordinate along water-flow direction; see (VII.1)
Λ_c	critical "scallop" wavelength $2\pi/m_c$, for which scallops have the maximum growth rate (ω_c); see (VIII.7)
λ	scaled size of grains of mineral A; see (A.15), app. A
μ	normal velocity of reaction front in scaled time units; see (VI.8)

TABLE 1

(Continued)

μ_w	viscosity of water in the Fair-Hatch equation, (VIII.8)
ν	scaled water velocity; see (A.9)
ξ	cube root of ratio of grain density numbers for minerals B and A; see (IX.A12)
ρ_A, ρ_w	molar density of mineral A and water (moles/cm^3)
ϕ	local porosity
ϕ_0	porosity of the unaltered rock
ϕ_f	porosity of the altered rock, after dissolution of grains of mineral A
ω	growth rate (in sec^{-1} of scaled time) of "scallops" of wavelength Λ in the reaction front; see (VIII.3); $\delta\omega$, growth rate in *real* sec^{-1}
ω_c	the maximum growth rate, which corresponds to reaction-front "scallops" having the critical wavelength Λ_c; see (VIII.5, 6)
τ	scaled time; see (VI.2)
$\underline{\eta}$	dimensionless front velocity introduced in app. A
$\bar{}$	overbar; designates a value of a variable for the planar front; see (VIII.1)
$\hat{}$	designates amplitude of variables $\tilde{S}$, $\tilde{\gamma}$, $\tilde{p}$; see (III.1)
$\tilde{}$	designates characteristic constants of the system in section IX and small deviations elsewhere

I. INTRODUCTION

Reactive water that flows through a porous rock establishes a moving reaction front within it. As we show below, the front can spontaneously become regularly scalloped even in rocks having initially uniform texture. Suppose that X is an aqueous species brought in by the water and A is a mineral disseminated in the rock, and assume that X and A react through the irreversible process

$$X_{(aq)} + A_{(s)} \rightarrow \text{aqueous products.} \qquad (I.1)$$

A common example is the oxidative dissolution of pyrite. Assume the other minerals in the rock do not react with the incoming aqueous solution under the prevailing conditions. An A-dissolution front moves slowly downflow driven by the input of X dissolved in the water and divides the rock into two regions: in the region downflow from the front, mineral A is still unreacted, whereas in the region upflow from it, A has already been dissolved out. The front itself is a transition zone whose thickness depends on the kinetics of reaction (I.1) and on the characteristics of the transport mechanisms involved.

Several questions arise regarding the evolution of the system: what are the velocity, shape, and thickness of the front? What are the spatial distributions of permeability, porosity, modal amount of A, and water composition at any given time?

The purpose of this article is to answer these questions by means of a quantitative model of the reaction-transport system outlined above. A key element of the phenomenon and of the model is what we call the *reactive-infiltration feedback.* Both this feedback and the modeling approach applied here are presented in part I of this series on geochemical self-organization (Ortoleva and others, 1987).

The reactive-infiltration feedback works as follows. Consider a porous rock with an imposed inlet flow as in figure 1. The heavy line

indicates the position of the A dissolution front at a given time. The permeability in the vicinity of a point within the bump is higher, because A has been dissolved out there. This focuses the flow of X-bearing reactive water to the tip of the bump, causing it to become longer. Clearly this process of front bump growth is an example of positive feedback, as discussed in section III.B and figures 1 to 3 of the first article in this series (Ortoleva and others, 1987).

The reactive-infiltration instability may also cause a planar front to become regularly scalloped, as follows. The capture of lateral flow by one point from another in the rock only takes place effectively if the two points are sufficiently close to each other. But if the two points are very close to each other, then diffusion makes the concentration of X the same in them, and the feedback is terminated. From this we expect, and demonstrate explicitly below, that a favored wavelength (or scallop spacing) should emerge. Geological examples of scalloped fronts are given in the next section. The basis for the modeling of reaction front scalloping given in this article is in our general article on self-organization. Other efforts at modeling reaction-transport interaction are, for example, those of Nguyen and others (1982), Rubin (1983), Kirkner, Jennings, and Theis (1985), Hill (1978), and Schecter and Gidley (1969), though these do not include feedbacks.

The mathematical model below consists of continuity equations for solutes and water, a rate equation for mineral dissolution, and Darcy's law. The morphological stability of the front is studied by linear analysis. Nonlinear effects are taken into account by direct numerical simulation of the system of dynamical equations. The main result of the morpho-

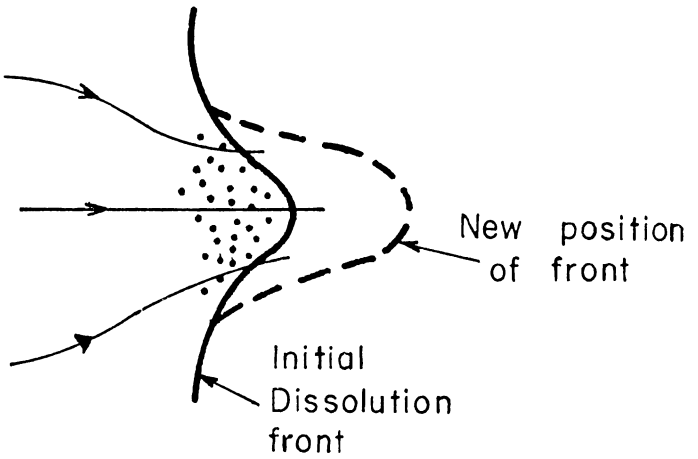

Fig. 1. Dissolution front (heavy line) moving downflow in a porous rock with generally horizontal inlet water flow from the left. The reactive water is focused to the tip of the dissolution bump increasing the rate of dissolution there and hence extending the bump.

logical stability analysis is that a dissolution front that is initially roughly planar indeed becomes scalloped as it moves downflow.

Some experimental evidence for the operation of reactive infiltration feedback is given by Schecter and Gidley (1969) and Hill (1978). These experiments and the observations and the quantitative kinetic model described in detail below strongly warrant considering the reactive-infiltration feedback as an important mechanism in water-rock interaction. In particular, the spontaneous, autonomous ability of moving aqueous solutions to dissolve out higher-permeability fingers in sedimentary rocks emerges as a significant concept in the compaction and diagenesis of sedimentary basins and hydrocarbon migration.

The mathematics of the reactive-advection problem is complex. Solving the problem involves obtaining results on a number of coupled, nonlinear partial differential equations. In order to obtain analytical results we have restricted the chemistries to two simple cases, but without losing the essential features of the reactive-infiltration feedback. Indeed this reactive-infiltration feedback is a universal feature that only depends on the overall nature of the reaction network and not on the detailed chemical steps and speciation. This "universality" has, in fact, been a general conclusion of the research of the past two decades on other self-organization phenomena in reaction-transport systems (see Nicolis and Prigogine, 1977). It is our hope that this article promotes awareness of the reactive-infiltration feedback and related self-organization phenomena. In particular we hope that quantitative geological and experimental data can be made available that will warrant further modeling studies incorporating the more complex chemistries of realistic mineral dissolution and aqueous reaction processes.

II. SCALLOPED FRONTS IN NATURE

The following examples of scalloped fronts occur in rocks where one can be reasonably sure that significant alteration has taken place driven by an imposed flux of reactive aqueous fluids.

A. Siltstones of the deltaic Paleozoic Borden Group of Southern Indiana (USA) and sandstones of the Nubia Sandstone in southern Jordan and the Sinai Peninsula commonly contain well scalloped redox surfaces marked by sharp color changes. The scallops are centimeters apart. One example is shown in figure 2.

B. Uranium roll front deposits have been described by, among others, Galloway (1978) and Bailey and Childers (1977) as consisting of tongues with wavelengths of 1 to 10 km in map view. In cross section the rolls may be separated by as little as a few meters.

C. In thick weathering alteration profiles of manganese-rich sedimentary rocks of Gabon, Nahon (personal commun., 1985) has described fingered surfaces, which he calls "glove-shaped," separating alteration regions with and without rhodochrosite. The fingers are about 25 cm apart (see fig. 3).

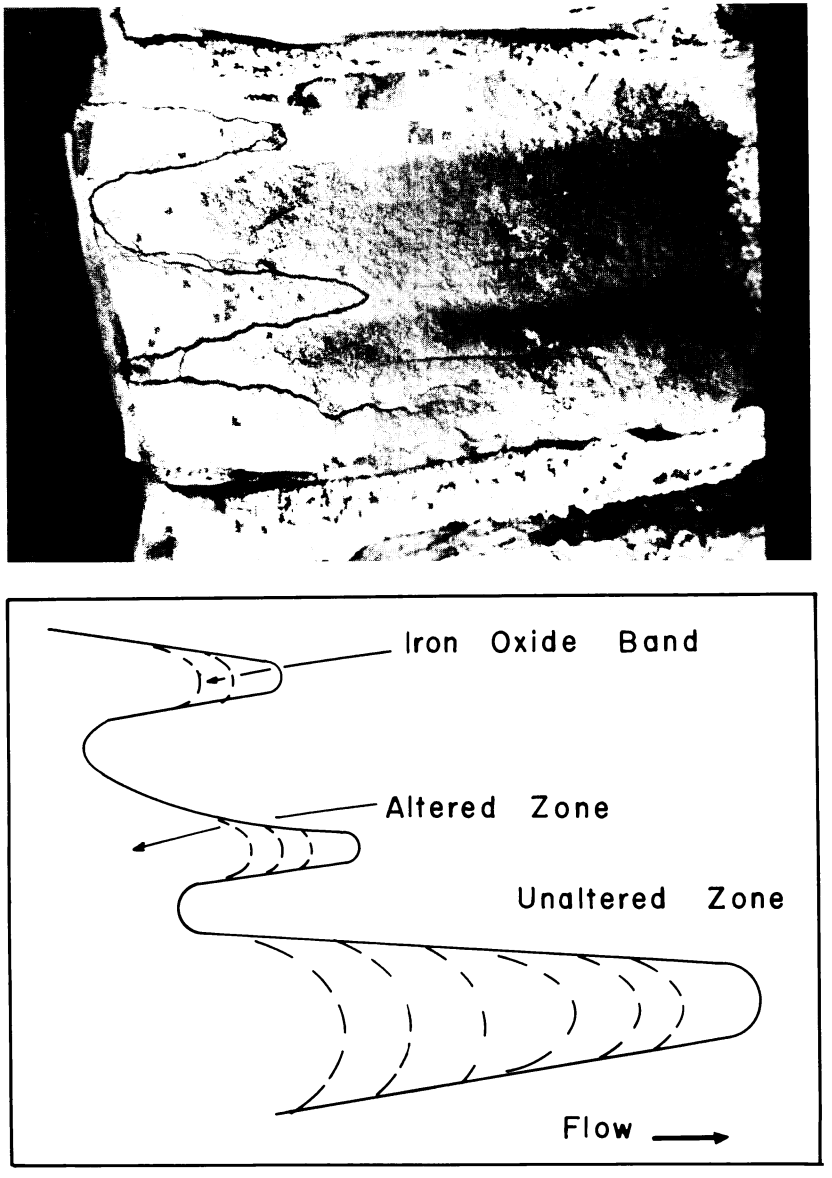

Fig. 2. Scalloped reaction front with trace from a photograph of a loose block of the Borden Group, Bloomington, southern Indiana. The wavelength of the scallops is 5 to 6 cm. Bedding is shown by the dotted lines. Because of the iron oxide bands indicated by dashed lines, the water is inferred to have flowed to the right.

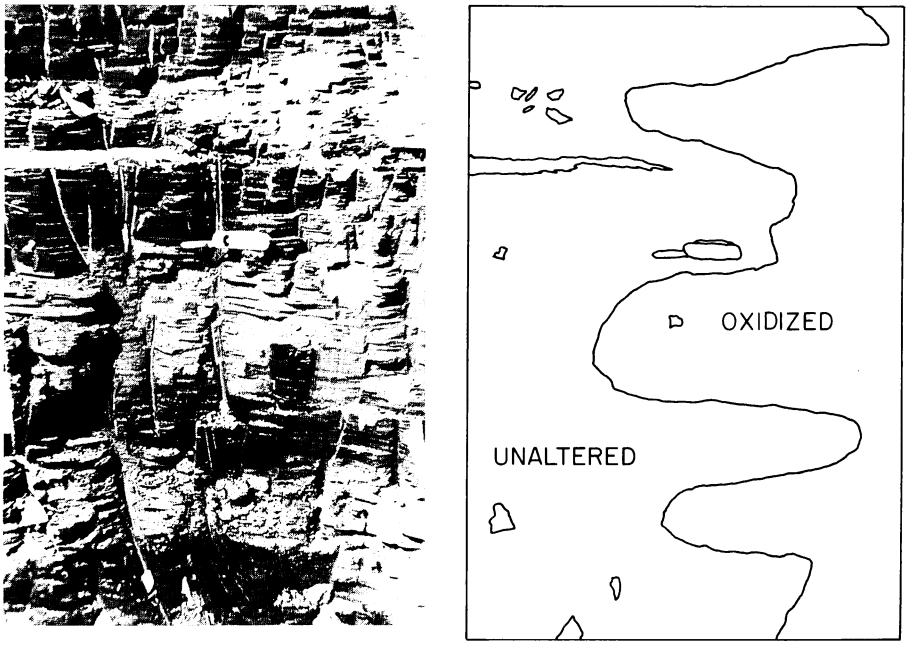

Fig. 3. Scalloped reaction front (with trace from a photograph taken by D. Nahon, Univ. Marseille) separating an altered rhodocrosite-free zone from the unaltered zone in a weathering profile on Mn-rich rocks of Gabon. Wavelength is about 25 cm.

D. Some skarns consist of alternating mineral bands that are scalloped. One example from Primorye (Maritime Provinces, eastern USSR) is shown in figure 4.

E. When all the minerals in a rock are soluble in the aqueous solution flowing through it, the reaction-infiltration instability may cause "worm holes" instead of scalloped fronts. Worm holes are common in karstified limestones (see fig. 5) and occur also in quartz arenites subjected to alkaline weathering conditions (fig. 6).

While detailed petrological analyses of these textures should be carried out to prove they have resulted from the reactive-infiltration instability, it appears that they are examples of geochemical self-organization to be added to those surveyed in Merino (1984).

III. REACTION MECHANISMS

The spontaneous scalloping, or fingering, of reaction fronts often observed in water-rock systems may be interpreted in terms of geochemical self-organization. Self-organization is the autonomous, spontaneous passage of a system from an unpatterned to a patterned state in the absence of externally imposed *periodic* causes. The essential role of nonequilibrium conditions and fluctuations in causing self-organization is given in part I of this series. For the present problem the unpatterned

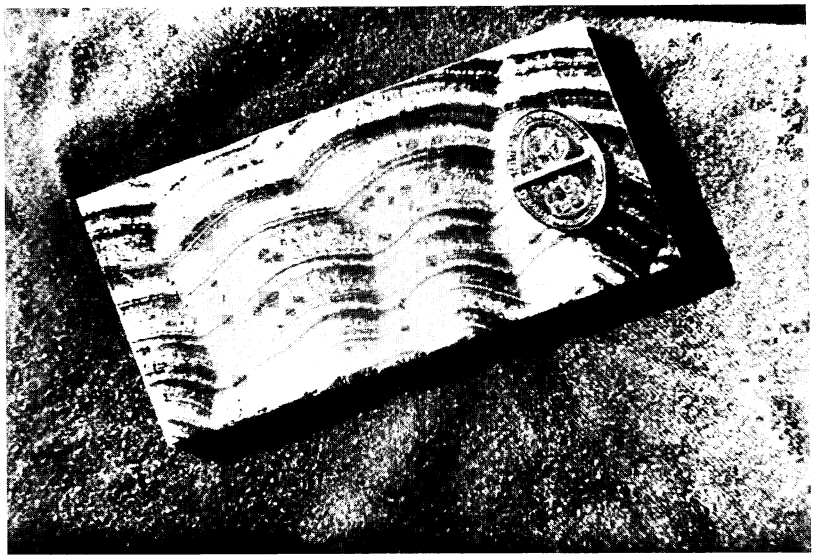

Fig. 4. Scalloped mineral bands of datolite, wollastonite, and hedenbergite in a skarn from Primorye, easternmost USSR. Wavelength is about 3 cm. (Sample provided by D. Rousell.)

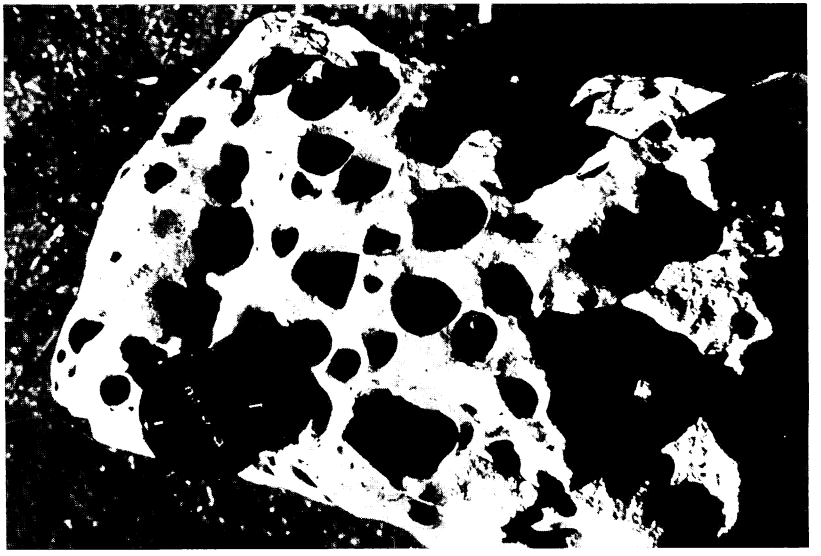

Fig. 5. Evenly spaced dissolution holes in karstified Miocene lacustrine limestone from Madrid, Spain. Field of view is 60 cm.

Fig. 6. Dissolution holes in a ferruginous quartz arenite from Moanda (Gabon). The dissolution took place under tropical, alkaline weathering conditions (Nahon, personal commun., 1985).

state is the planar reaction front, whereas patterning consists of the spontaneous development of scalloping of this reaction zone.

A. Active versus passive dissolution.—Many reaction schemes aside from (I.1) can sustain non-equilibrium reaction zones and therefore satisfy a necessary condition for self-organization. Consider the passive dissolution of a mineral A into a solute Y:

$$A_{(s)} \rightleftharpoons Y_{(aq)}. \qquad \text{(III.1)}$$

When A-undersaturated water flows through A-bearing rock, an A-dissolution front moves downflow. The fluid in the zone downflow from the front reaches a Y concentration in equilibrium with A. Although the passive dissolution (III.1) is different from the active dissolution (that is, a reactant is required in the inlet fluid), (I.1), the reaction-infiltration feedback operates just the same. In fact we shall show that the mathematical reaction-transport models for reactions (I.1) and (III.1) are identical.

More complicated variants of the basic reactions (I.1) or (III.1) are the rule in geological systems, wherein many mineral and solutes can react simultaneously. Multimineralic systems can lead to interesting phenomena, as when one mineral precipitates at the dissolution front of another—a case in point being the formation of uranium-bearing minerals at a pyrite oxidative dissolution front.

B. Self-promoting mechanisms.—Consider a case where a mobile agent Z promotes its own production via the consumption of a mineral A and a molecule X:

$$X + Z + A_{(s)} \rightarrow 2Z. \qquad \text{(III.2)}$$

As an example of the general process (III.2) Z represents a bacterium, the incoming fluid contains a nutrient X required for metabolism, and A represents solid carbonaceous material. If Z is present in the inlet and absent in the unaltered rock, then the Z production-A consumption front moves downstream. In contrast, if Z is absent in the inlet and present far downstream, then a Z front can move *upstream* under certain conditions as in figure 7 (Ortoleva, in press). Thus a novel feature of self-promoting mechanisms is that they allow for reverse fronts.

A geological engineering analog of this is the *in situ* gasification of coal, a case that involves oxygen (X) flowing in while the flame front—"autocatalytic" with respect to the temperature (Z)—moves upstream if initially ignited far downstream (Britten and Krantz, 1984) (that is, the exothermicity of the reaction increases local temperature which, in turn, increases local reaction rate through the temperature dependence of the rate coefficients). Models of these gasification fronts show that scalloping can occur due to temperature effects even in the absence of porosity changes. Since the burning of the hydrocarbons does increase the porosity, it is clear that the system has two morphological instability mechanisms acting simultaneously.

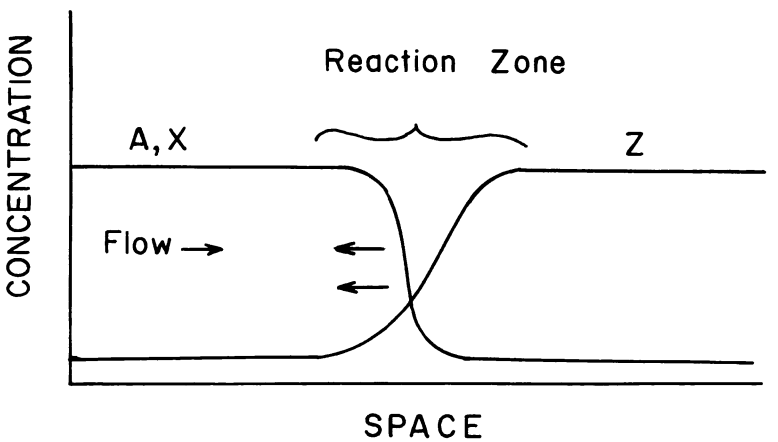

Fig. 7. Schematic profiles (moles/rock volume versus space) of mobile species X and Z and mineral A for the autocatalytic process $X + Z + A \rightarrow 2Z$ (III.2), showing a reaction front that moves against the flow.

IV. DYNAMICAL EQUATIONS OF REACTIVE INFILTRATION

This section gives the equations modeling the reactive-infiltration feedback for the processes (I.1) and (III.1). The two models are shown to be mathematically equivalent.

A. The X + A → Products Model

Consider the reaction (I.1) to take place in a tabular, subhorizontal sandstone body sandwiched between shales. Mineral A is initially uniformly distributed throughout the sandstone. X-rich water flows through the sandstone driven by a pressure gradient. We assume that the disseminated A grains are sufficiently scarce that even after they are completely dissolved out the rock is still self-supporting. The other component of the sandstone, mineral B, is taken to be essentially insoluble in the X-bearing water. Porosity and permeability are assumed to be initially uniformly distributed. The local flow is thus initially equal everywhere and so is therefore the local rate of A dissolution at all points in a plane perpendicular to the flow. Soon, however, small, omnipresent initial random deviations of porosity start to attract increasing amounts of X flux through the reactive infiltration feedback described in the Introduction.

The equations governing the dynamics of this feedback process are (see Chadam and others, 1986) (A) the conservation of reactant X, (B) the condition of water conservation, (C) the rate of grain dissolution, (D) a volume condition relating the porosity to other texture variables, and (E) Darcy's law. These five equations can be written respectively as:

$$\frac{\partial(\phi X)}{\partial t} = -\vec{\nabla} \cdot \vec{J} + n_A \rho_A \frac{\partial L_A^3}{\partial t} \tag{IV.2}$$

$$\frac{\partial(\phi \rho_w)}{\partial t} = -\vec{\nabla} \cdot (\phi \rho_w \vec{v}) \tag{IV.3}$$

$$\frac{\partial L_A^3}{\partial t} = -k L_A^2 X \tag{IV.4}$$

$$\phi + n_A L_A^3 + n_B L_B^3 = 1 \tag{IV.5}$$

$$\vec{v} = -\kappa(\phi)\vec{\nabla} p \tag{IV.6}$$

where X and $\vec{J}$ are the concentration (in moles/unit of pore volume) and flux (in moles per sec per cm^2 of rock cross section); ϕ is the porosity in a small volume, ΔV, of sandstone about a given observation point $\vec{r}$ in the rock, ΔV is small enough that $(\Delta V)^{1/3} \ll$ typical length of the pattern to be described but large enough to contain, say, 100 or 200 grains. L_A^3 and L_B^3 are the volumes of A and B grains, and n_A and n_B are the grain number densities of A and B (number of grains per unit volume). ρ_w is the molar density of water, assumed to be constant; $\vec{v}$ is the water

velocity; $\kappa(\phi)$ is the permeability (of a small rock volume ΔV) divided by the water viscosity; and $\vec{\nabla}p$ is the fluid pressure gradient. Eqs (IV.2,3) are statements of the continuity equation (for example, De Groot and Mazur, 1962); they establish that, for each small rock volume ΔV, the rate of variation of mass of X and water, respectively, equals the instantaneous rate of material transported into ΔV plus the instantaneous amount created through reaction with ΔV. Eq (IV.4) is the rate of reaction (I.1) for one grain of A. This rate is taken here to be first order in the surface area and the X concentration (though any rate expression that vanishes with both L_A and X will yield essentially the same results as those obtained in this paper); k is the reaction-rate constant. Assuming all A grains in any given small volume ∇V to have the same volume L_A^3, taking the flux due to diffusion and flow to be $\vec{J} = -\phi D(\phi)\vec{\nabla}X + \phi X\vec{v}$, with $D(\phi)$ being the effective diffusion coefficient in the porous rock, and letting ϕ_f be the porosity after all A has been dissolved out, (that is, $\phi_f = 1 - n_B L_B^3$), the dynamical eq (IV.2–6) become

$$\frac{\partial(\phi X)}{\partial t} = \vec{\nabla} \cdot [\phi D(\phi)\vec{\nabla}X + \phi X\kappa(\phi)\vec{\nabla}p] - \rho_A \frac{\partial \phi}{\partial t} \tag{IV.7}$$

$$\vec{\nabla} \cdot [\phi\kappa(\phi)\vec{\nabla}p] - \frac{\partial \phi}{\partial t} = 0 \tag{IV.8}$$

$$\frac{\partial \phi}{\partial t} = -k n_A^{1/3} (\phi_f - \phi)^{2/3} X. \tag{IV.9}$$

Eqs (IV.7–9) constitute a simple closed system of equations in X, ϕ, and p that captures the essence of the reactive-infiltration feedback.

Assuming now that the overall direction of advancement of the A-dissolution front is the horizontal z axis, eqs (IV.7–9) are to be solved for the following boundary conditions:

$$\left.\begin{aligned} \phi &= \phi_0 \\ X &= 0 \end{aligned}\right\} \text{for } z \to +\infty \text{ (that is, far ahead of the front)}$$

$$\left.\begin{aligned} \phi &= \phi_f \\ X &= X_M \\ -\kappa_f(\partial p/\partial z) &= v_f \end{aligned}\right\} \text{for } z \to -\infty \text{ (that is, far behind the front)} \tag{IV.10}$$

where X_M is the X concentration in the incoming water, v_f and κ_f are, respectively, the water infiltration velocity and value of κ after dissolution of A, and ϕ_0 is the porosity far downstream from the reaction front. Thus a complete description of the reaction front requires solution of the mathematical problem (IV.7–9) subject to the boundary conditions (IV.10).

B. The A ⇌ Y Model

A reaction-infiltration model for reaction (III.1) may be constructed similarly to that presented for the process X + A → products. Interestingly a simple transformation can be used to show that the two are mathematically equivalent. Eqs (IV.3,5,6) stand, while (IV.2,4) now become

$$\frac{\partial \phi Y}{\partial t} = \vec{\nabla} \cdot [\phi D(\phi) \vec{\nabla} Y - \phi Y \vec{v}] - n_A \rho_A \frac{\partial L_A^3}{\partial t} \tag{IV.11}$$

$$\frac{\partial L_A^3}{\partial t} = k L_A^2 [Y - Y^{eq}] \tag{IV.12}$$

where Y^{eq} is the saturation value of Y. Note the change in sign in the last term of (IV.11) from that in (IV.2) due to the fact that in (I.1) A dissolution consumes X while in (III.1) it liberates Y. Consider now the change of variables

$$Y = Y^{eq} - X. \tag{IV.13}$$

With this (IV.11) becomes, using (IV.3,6,8),

$$\frac{\partial \phi X}{\partial t} = \vec{\nabla} \cdot [\phi D(\phi) \vec{\nabla} X - \phi X \vec{v}] + n_A \rho_A \frac{\partial L_A^3}{\partial t}. \tag{IV.14}$$

Furthermore (IV.12) becomes (IV.4). Thus the X + A → products and A ⇌ Y models are mathematically equivalent. In the developments to follow we shall use the X + A → products model but keep in mind that the results apply to both models.

V. PLANAR CONSTANT-VELOCITY REACTION FRONTS

If the initial porosity were *exactly* the same in every ΔV of the sandstone, everywhere then for the constant cross section, lossless aquifer, the velocity of a planar dissolution front may be calculated from the dynamical equations. For this it is convenient to change coordinates to a reference system moving with the front; assuming the front to be moving along the z axis with velocity $\bar{u}$, the front fixed coordinate ζ is defined by

$$\zeta = z - \bar{u}t. \tag{V.1}$$

For the constant velocity front we regard the porosity, pore fluid concentration, and pressure (ϕ, X, and p) to be functions of ζ. Bearing in mind that

$$\partial \zeta / \partial z = 1 \text{ and } \partial \zeta / \partial t = -\bar{u}, \tag{V.2}$$

and putting $X(\zeta)$, $\phi(\zeta)$, and $p(\zeta)$ into the reaction-infiltration eqs (IV.7–9), we obtain

$$\frac{d}{d\zeta}\left[\phi D\frac{dX}{d\zeta} + \phi\kappa X\frac{dp}{d\zeta} + \bar{u}\phi(X + \rho_A)\right] = 0 \tag{V.3}$$

$$\bar{u}\frac{d\phi}{d\zeta} + kn_A^{1/3}(\phi_f - \phi)^{2/3}X = 0 \tag{V.4}$$

$$\frac{d}{d\zeta}\left[\phi\kappa\frac{dp}{d\zeta} - \bar{u}\phi\right] = 0. \tag{V.5}$$

Since the bracketed quantities in (V.3,5) are constant, we can evaluate them far behind and far ahead of the front (using the boundary conditions (IV.10)) and then equate the two expressions: we obtain

$$\bar{u} = \frac{\phi_f X_M}{\phi_f X_M + (\phi_f - \phi_o)\rho_A} v_f. \tag{V.6}$$

This expression gives the velocity of the planar front $\bar{u}$ as a fraction of the inlet water velocity v_f (that is, the water velocity far behind the A-dissolution front). The fraction in (V.6) reflects the 'buffering capacity' of the rock on account of its A content. Indeed the higher the molar concentration of A per rock volume, $(\phi_f - \phi_0)\rho_A$, the slower the front velocity.

The above result (and a similar one yielding the flow velocity far downstream) simply reflects overall mass balance and does not depend on the details of the dissolution kinetics or diffusive or advective transport. In contrast, the *profiles* of X, ϕ, and p within the reaction zone do depend on the details of the dissolution and transport rate laws. For the reversible reaction (III.1) the result (V.6) stands, provided X_M is replaced by $(Y^{eq} - Y_M)$ where Y_M is the inlet value of Y. Similar results may be obtained for reactions containing several aqueous reactants and products; in these cases the front velocity depends on the aqueous concentrations in the inlet fluid, initial mineral content, flow velocity, and equilibrium constant for the reaction.

VI. THE REACTION FRONT DYNAMICS AS A FREE BOUNDARY PROBLEM

The solution of the model (IV.7–9) for the boundary conditions (IV.10) yields the temporal development of the spatial distribution of the concentration of X, porosity, and fluid pressure. An important natural constraint on the equations is that the density of minerals is always orders of magnitude greater than the concentrations of solutes in aqueous solutions, at least under diagenetic conditions (Ortoleva and others, 1987). For example, the density of pyrite is 0.0417 moles/cm^3, and the low-temperature saturation concentration of oxygen in water at 1 atm is ~10 ppm = 3×10^{-7} moles/cm^3; the ratio

$$\delta \equiv X_M/\rho_A \tag{VI.1}$$

is $\sim 10^{-5}$. Thus, our task is to solve the dynamical eqs (IV.7–9) for very small δ. As described in part I of this series, the constraint $\delta \ll 1$ can be turned to advantage by explicitly introducing δ into the equations. In the present problem we can do this scaling concentration and time according to

$$\begin{aligned} \gamma &= X/X_M \\ \tau &= \delta t \,. \end{aligned} \tag{VI.2}$$

The quantity γ then is a dimensionless concentration variable between 0 and 1. The reason to define the new time τ is that the reaction front must move very slowly. From (V.6), for small δ we have

$$\bar{u} = \frac{\phi_f}{\phi_f - \phi_0}\,\delta v_f. \tag{VI.3A}$$

Thus, as τ changes by one unit, t changes greatly because $\delta \ll 1$; to travel a length of geological interest, the front needs a characteristic time that increases as δ^{-1} as δ gets small.

In general the transition zone over which the porosity changes from ϕ_f behind the front to ϕ_0 ahead of it has a finite thickness Δ which is calculated in app. A for model (III.1); we find

$$\Delta \simeq [\delta D t_d\,(L^3_{A,0})]^{1/2}, \tag{VI.3B}$$

where $t_d(L^3_{A,0})$ is the lifetime of an A grain of volume $L^3_{A,0}$ in a water devoid of Y. For $\delta \ll 1$ the front is therefore very thin, and in the limit $\delta \to 0$ it is infinitesimally thin and can be regarded as a surface across which the porosity jumps from ϕ_f to ϕ_0. Let that surface (the dissolution front) be the locus of points $\vec{r}$ where a function S vanishes,

$$S(\vec{r}\,, \tau) = 0 \text{ at the dissolution front.} \tag{VI.4}$$

We take $S > 0$ in the region ahead of the front and $S < 0$ in the altered zone. Inserting (VI.1, 2) into the dynamical eqs (IV.7–9), and, since δ is small, neglecting terms proportional to δ, δ^2, et cetera, we get

$$D_f \nabla^2 \gamma + \kappa_f \vec{\nabla}\gamma \cdot \vec{\nabla} p = 0, \; S < 0 \tag{VI.5}$$

$$\begin{aligned} \gamma &= 0, \; S > 0 \\ \nabla^2 p &= 0, \; S \neq 0 \end{aligned} \tag{VI.6}$$

where D_f and κ_f are the diffusion coefficient and permeability to viscosity ratio evaluated for the porosity ϕ_f. The two differential eqs (VI.5, 6) are to be solved in a spatial domain one of whose boundaries, the dissolution front $S = 0$, is itself unknown in speed and location and that must be determined self-consistently with the temporal development of the spatial distribution of the X concentration and the pressure. Such mathematical problems are called free boundary, or Stefan, problems (for example, Rubinstein, 1971; Ockendon and Hodgkins, 1975; Rubin,

1983; Schmidt and Ortoleva, 1980, 1981; Chadam and Ortoleva, 1986). Their resolution requires an additional condition, which in our case is an equation of motion for the dissolution interface function S,

$$\frac{\partial S}{\partial \tau} + \mu|\vec{\nabla} S| = 0, S = 0, \tag{VI.8}$$

obtained as shown in app. B; μ is the normal front velocity in the present time units and is still to be determined; $\delta\mu$ is the actual velocity.

The free boundary problem for the dissolution front dynamics is mathematically completed by deriving the boundary conditions for γ and p at the reaction front as follows:

1. The water pressure must be the same immediately upstream (0^-) and downstream (0^+) of the front, that is

$$p|_{0^-} = p|_{0^+}. \tag{VI.9}$$

2. Water must be conserved across the front, and, because it is incompressible (see app. C),

$$\left.\frac{\partial p}{\partial n}\right|_{0^-} = \Gamma \left.\frac{\partial p}{\partial n}\right|_{0^+}, \tag{VI.10}$$

where $\partial/\partial n$ is the spatial derivative normal to the surface $S = 0$, and

$$\Gamma \equiv \phi_0 \kappa_0 / \phi_f \kappa_f \tag{VI.11}$$

expresses the contrast in the $\phi\kappa$ product across the reaction front.

3. At the front the concentration of X vanishes:

$$\gamma|_{0^-} = 0 \tag{VI.12}$$

because X is consumed by reaction with mineral A.

4. In the reference frame moving with the front, the influx of X coming from upstream into the front must be just balanced by the influx of mineral A coming in from the downstream side of the front,

$$\phi_f D_f \left.\frac{\partial \gamma}{\partial n}\right|_{0^-} = \mu(\phi_f - \phi_0). \tag{VI.13}$$

The influx of X into the moving front from upstream is only due to diffusion (since $\gamma = 0$ at the front) and is

$$-\phi_f D_f \left.\frac{\partial \gamma}{\partial n}\right|_{0^-},$$

which is the left side of (IV.13). The influx of mineral A into the front from downstream is the front velocity μ times the initial modal amount of A. Since ϕ_0 and ϕ_f are the porosities before and after dissolution of A, the initial mode of A is $\phi_f - \phi_0$.

5. Finally, the boundary conditions far upstream of the front are

$$-\kappa_f \frac{\partial p}{\partial z} \rightarrow v_f \text{ as } z \rightarrow -\infty. \tag{VI.14}$$

$$\gamma \rightarrow 1 \text{ as } z \rightarrow -\infty. \tag{VI.15}$$

With this we have converted the reaction front dynamics into a free-boundary problem valid for $\delta \ll 1$. We now turn to the solution of (VI.5,6) for the case of a planar front. Scalloping of the front is studied in section VIII.

VII. CONCENTRATION AND PRESSURE PROFILES FOR THE PLANAR FRONT

In this section we analyze the planar front via the $\delta \rightarrow 0$, free boundary approximation of the previous section. Consider a planar front propagating along the z axis with velocity $\bar{\mu}\tau$ and introduce the coordinate ζ moving with the front.

$$\zeta = z - \bar{\mu}\tau \tag{VII.1}$$

We fix the porosity discontinuity at $\zeta = 0$ and for convenience fix the pressure reference so that $p(\zeta)$ vanishes at $\zeta = 0$: we have the freedom to do this because in a porous flow problem in which the fluid is incompressible only relative pressure is important. Letting quantities in the planar front be indicated by a bar, we can now solve the system of eqs (VI.5,6) in one spatial dimension with the boundary conditions (VI.9,10,12–15). The solution is (see app. D)

$$\bar{p} = \begin{cases} p_0'\zeta \\ p_f'\zeta \end{cases}, \quad \bar{\phi} = \begin{cases} \phi_0 \\ \phi_f \end{cases}, \quad \bar{\gamma} = \begin{cases} 0 \\ 1 - e^{\alpha\zeta} \end{cases}, \quad \text{for} \begin{cases} \zeta > 0 \\ \zeta < 0 \end{cases}, \tag{VII.2}$$

where

$$\alpha = v_f/D_f, \tag{VII.3}$$

$$-\kappa_f p_f' = v_f, \; p_0' = p_f'/\Gamma. \tag{VII.4}$$

at $-\infty$ and $+\infty$ respectively. The profiles (VII.2) are shown in figure 8.

The velocity $\bar{\mu}$ of the planar front can be obtained from the boundary condition (VI.13) combined with $\bar{\gamma} = 1 - e^{\alpha\zeta}$ in (VII.2) and with (VII.3). The result if

$$\bar{\mu} = \phi_f v_f/(\phi_f - \phi_0). \tag{VII.5}$$

This equation is identical to the one derived by dividing (V.6) by δ, letting $\delta \rightarrow 0$, and noting that the change of time scale according to (VI.3A) implies that $\bar{\mu} = \delta\bar{\mu}$.

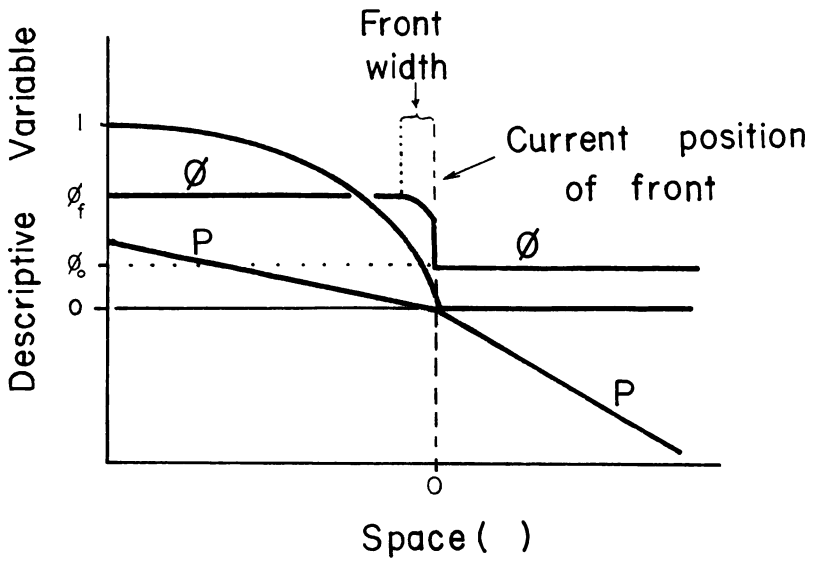

Fig. 8. Scaled X concentration γ, pressure p, and porosity ϕ as obtained from the solid density asymptotics of section VIII for the planar dissolution front. While the ϕ-front thickness is strictly zero in the infinite solid-density asymptotic limit it is drawn here as being finite for illustrative purposes.

VIII. MORPHOLOGICAL INSTABILITY OF THE PLANAR REACTION FRONT

A. Linear Stability Analysis

A central result of the present paper is the demonstration (by linear stability analysis—for example, Chandrasekhar, 1961) of the instability of the planar reaction front to the formation of "scallops" or fingers. As in other problems involving the morphological stability of moving interfaces in first-order phase transitions (for example, Sekerka, 1967; see also Chadam and others, 1986), we study deviations from the planar front by writing each relevant variable as the sum of the corresponding value for the planar front plus a deviation from it:

$$\begin{aligned} p &= \bar{p} + \tilde{p}(y, \zeta, \tau), \\ \gamma &= \bar{\gamma} + \tilde{\gamma}(y, \zeta, \tau), \\ S &= \bar{S} + \tilde{S}(y, \tau) \text{ (where } \bar{S} = \zeta). \end{aligned} \tag{VIII.1}$$

Thus we consider variations along y, which is perpendicular to the top and bottom of the aquifer and to the ζ-direction along which the planar front advances. (For simplicity we neglect here variations along the x direction, that is, the strike of the bed.) The linear stability analysis proceeds by inserting these expressions into the full free boundary problem of section VI and only keeping terms *linear* in the deviations.

(Nonlinear effects on the instability are considered in section IX.) One finds solutions in the form

$$\begin{aligned} \tilde{S}(y, \tau) &= \hat{S}e^{\omega\tau} \cos my \\ \tilde{\gamma}(y, \zeta, \tau) &= \hat{\gamma}(\zeta)e^{\omega\tau} \cos my \\ \tilde{p}(y, \zeta, \tau) &= \hat{p}(\zeta)e^{\omega\tau} \cos my \end{aligned} \tag{VIII.2}$$

where $\omega(m)$ takes on the value (app. E)

$$\omega(m) = \frac{\phi_f v_f}{(\phi_f - \phi_o)(1 + \Gamma)} [\alpha + (1 - \Gamma)m - (\alpha^2 + 4m^2)^{1/2}]. \tag{VIII.3}$$

The quantities under the $\hat{}$ are the amplitudes of S, γ, and p; m is inversely proportional to the wavelength of the fingers developed by the reaction front ($m = 2\pi/\text{wavelength}$), and ω is the growth rate, in (scaled time units)$^{-1}$, of those fingers as a function of their wavelength. The growth rate in sec^{-1} is $\delta\omega$. The quantities α and Γ were defined before as $\alpha \equiv v_f/D_f$ (VII.3) and $\Gamma \equiv \phi_o\kappa_o/\phi_f\kappa_f$ (VI.11).

The dependence of ω on m given by (VIII.3) is crucial to understanding the dynamics of the system and is shown in figure 9. It is clear in (VIII.2) that, for perturbations (of the planar front) in S, γ, or p to grow

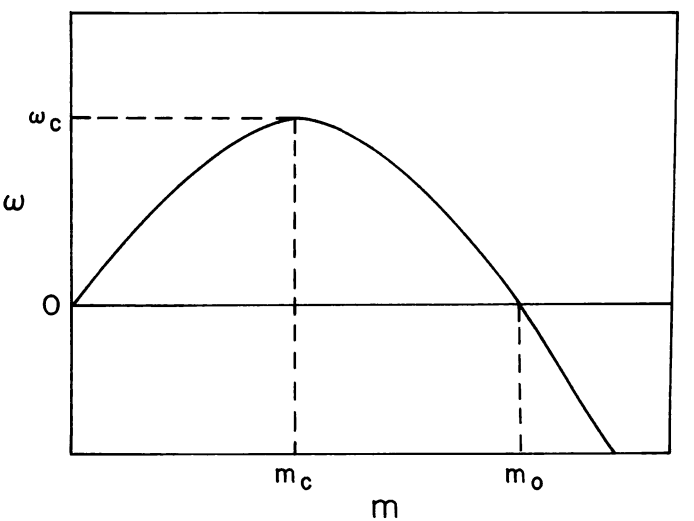

Fig. 9. Plot of the growth rate (ω) of reaction-front scallops as a function of m, which equals 2π divided by the wavelength of those scallops; see eq (VIII.3). The growth rate, ω, is positive for $0 < m < m_o$, where m_o is given by (VIII.4). ω is maximum for $m = m_c$ given by (VIII.5). Scallops with a wavelength $\lambda_c = 2\pi/m_c$ have the highest possible growth rate and are therefore the ones the dissolution front is expected to adopt in the early stages of front advancement.

with time, ω must be positive. Figure 9 shows that ω is positive in an interval $0 < m < m_o$ where

$$m_o = \frac{2(1 - \Gamma)\alpha}{(3 - \Gamma)(1 + \Gamma)}. \qquad \text{(VIII.4)}$$

The growth rate ω reaches a maximum at $m = m_c$; m_c is obtained by setting $d\omega/dm$ equal to zero:

$$m_c = \frac{(1 - \Gamma)\alpha}{2[(3 - \Gamma)(1 + \Gamma)]^{1/2}}. \qquad \text{(VIII.5)}$$

The corresponding maximum, ω_c, obtained by substituting (VIII.5) in (VIII.3), is

$$\omega_c = \frac{\phi_f D_f \alpha^2}{2(\phi_f - \phi_o)(1 + \Gamma)} \{2 - [(3 - \Gamma)(1 + \Gamma)]^{1/2}\}. \qquad \text{(VIII.6)}$$

This maximum growth rate is attained when the fingers are separated by $2\pi/m_c$. This analysis allows us to predict the spacing between the fingers or scallops of the dissolution front: banning atypical nonlinear effects (see sec. IX), we expect that wavelength of the scallops to be near $2\pi/m_c$ since perturbations with this wavelength grow the fastest. Note that for small porosity changes $\phi_f - \phi_o$ across the front, $\Gamma = \phi_o\kappa_o/\phi_f\kappa_f$ is close to unity, and hence m_c vanishes as $\phi_f - \phi_o$ vanishes. Thus even for very small porosity changes across the front the instability is still operative, but the wavelength and growth time of scallops becomes large. Indeed, as pointed out in section II, in uranium roll fronts the wavelength in map view can be of the order of 1 to 10 km (for example, Galloway, 1978). Note also that, when dissolution occurs at necks connecting pores (Hutcheon and Oldershaw, 1983), even small changes in porosity across the front may cause large changes in permeability and hence in Γ. Thus, the resulting spacing between fingers may be small even for small porosity changes across the front.

B. Predictions on Scalloping in Geological Systems

The linear stability analysis yields a relation (given by (VIII.3) and shown in fig. 9) between the growth rate of scallops, ω, and their wavelength, $\Lambda(=2\pi/m)$. Thus, the model allows us to predict that the dominant wavelength Λ_c in a given system will be the one corresponding to the scallops able to grow fastest. This is the behavior expected in the *early* stages of the evolution of an initially planar reaction front. Later, when well-defined fingers develop, we suppose that individual fingers competing with each other for the overall flow-through may eventually result in a giant finger. The numerical simulation of large fingers is discussed in the next section.

Since m in (VIII.3) equals $2\pi/\Lambda$, it follows from (VIII.5) that the probable wavelength adopted by a given system would be the critical

wavelength, given by

$$\Lambda_c = \frac{2\pi}{m_c} = \frac{4\pi D_f [(3 - \Gamma)(1 + \Gamma)]^{1/2}}{(1 - \Gamma)\, v_f}, \qquad \text{(VIII.7)}$$

where Γ is given by (VI.11).

The critical scallop wavelength Λ_c is shown in figure 10 as constant-Λ_c contours in terms of the initial A content ($n_A L_A^3 = \phi_f - \phi_o$) and final porosity ($\phi_f$). In all the plots of figure 9 we have assumed the

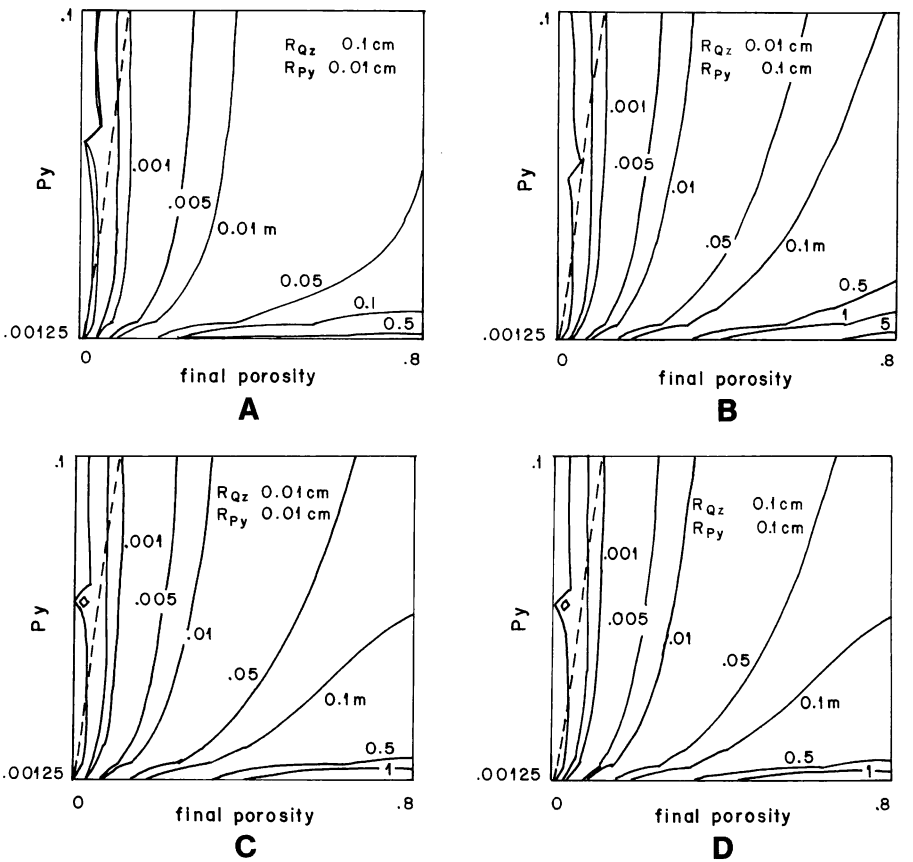

Fig. 10. Contours (in meters) of constant scallop wavelength in the initial volume fraction of pyrite (mineral A) versus final porosity plane, drawn with eq (VIII.7) for the Fair-Hatch formula (VIII.10). Only the region to the right of the heavy dashed line is physically meaningful, because $\phi_o = \phi_f - n_A L_A^3 > 0$, where ϕ_o, ϕ_f are the initial (downflow) and final (upflow) porosities. The initial grain radii are as indicated in each frame, and the inlet velocity is 10 m/yr. in all cases.

permeability and the porosity are related by the Fair-Hatch equation (Bear, 1972):

$$\kappa = \frac{\phi^3}{J\mu_w \theta^2 (1-\phi)^2}\left[\sum_i f_i L_i^{-1}\right]^{-2} \qquad \text{(VIII.8)}$$

where μ_w is the viscosity of water, θ is a geometric factor ($\theta = 6$ for spherical grains and $\theta = 7.7$ for angular grains), and J is a packing factor (≈ 5): L_i is the cube root of the volume of a grain of mineral i, and f_i is the fraction of the total grain volume occupied by grains of i. All grains of a given mineral at each point in space are assumed to have the same size. Thus we have

$$f_A = \frac{n_A L_A^3}{[n_A L_A^3] + [n_B L_B^3]}. \qquad \text{(VIII.9)}$$

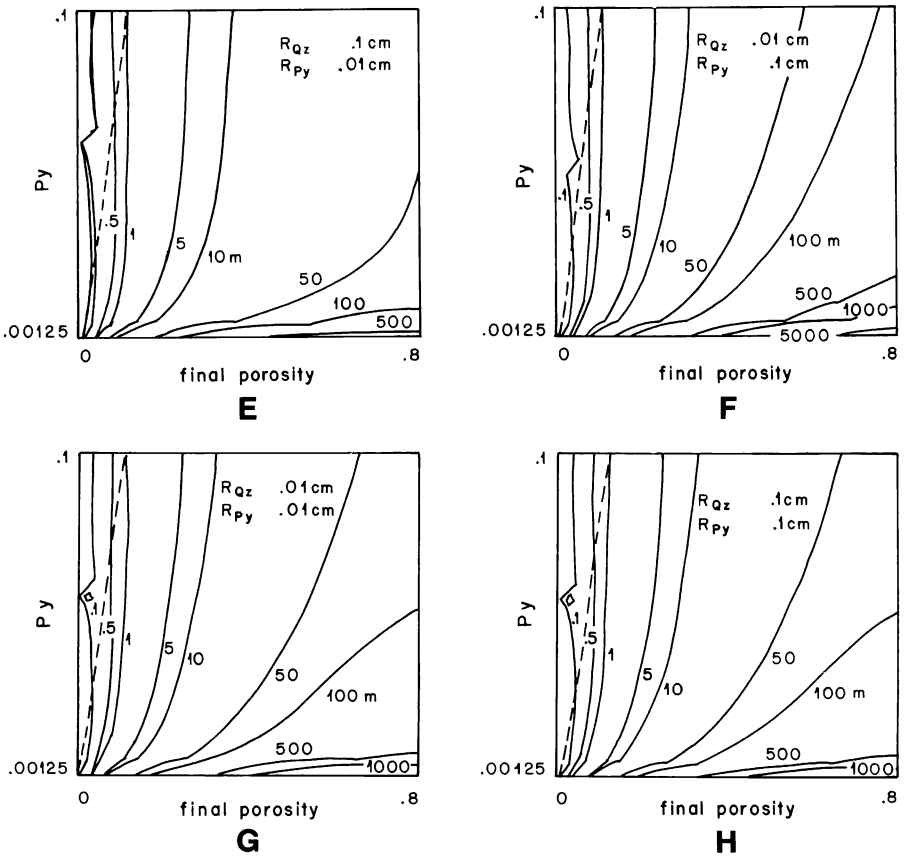

Fig. 10. (Continued)

Using eq (IV.5) and the post-alteration volume conditions

$$\kappa(\phi) = \frac{\phi^3}{J\mu_w\theta^2}\left[(1-\phi_f)^{2/3}n_B^{1/3} + (\phi_f-\phi)^{2/3}n_A^{1/3}\right]^{-2} \qquad \text{(VIII.10)}$$

Other $\kappa - \phi$ relations more appropriate to the rock of interest could be used instead. The diffusion coefficient $D(\phi)$ is taken to be of the form $D_o\phi^2$ where D_o is the diffusion coefficient in water (Lerman, 1979). All plots in figure 10 are for a bulk diffusion coefficient $D_o = 10^{-9}m^2/sec$. The water velocity through the altered zone has been taken as fast ($10m/yr \sim 3 \times 10^{-7}$ m/sec) or slow (1 cm/yr $\sim 3 \times 10^{-10}$). For each water velocity the A and B grain sizes have been chosen as both coarse, both fine, A coarse and B fine, and A fine and B coarse—see the captions of figure 10 for details. The water velocity strongly influences the scallop wavelength: Λ_c is inversely proportional to v_f. For the slow velocity scallop wavelengths are of the order of 5 km (for very low A modes and high ϕ_f) to 1 m for low ϕ_f. The fast velocity leads to wavelengths on the order of 1 m (for very low A modes and high ϕ_f to 1 mm for low ϕ_f). For A modes ≤ 0.6 percent the scallop wavelength is extremely sensitive to the A mode. For A contents >1 percent the wavelength depends mainly on ϕ_f, especially for $\phi_f < 40$ percent. All the contours are S shaped. Since A mode $\equiv n_A L_A^3 = \phi_f - \phi_o$ (see eq (IV.5) and combine it with $\phi_f + n_B L_B^3 = 1$), and because $\phi_o \geq 0$, it follows that in all the diagrams the physically accessible region is $n_A L_A^3 \leq \phi_f$, (or A mode $\leq$ final porosity), which is the region to the right of the dashed line on the plots of figure 10.

The predictions based on (VIII.7) and illustrated in figure 9 for a few specific combinations of geologically reasonable values of pertinent parameters yield finger wavelengths covering the range of observed ones, from a few centimeters to several kilometers (see sec. II).

IX. NUMERICAL SIMULATIONS

A. Dimensionless, Scaled Equations

The dynamics of reactive infiltration (IV.7–9) is nonlinear. The results of the linear stability analysis of section VIII demonstrate the morphological instability of the planar dissolution front, but to understand fully the dynamics of the reactive-infiltration feedback we have carried out numerical simulations of the nonlinear problem.

In order to make a given numerical simulation applicable to as large a body of physical data as possible, the simulations were done using the dynamical equations (IV.7–9), nondimensionalized according to (VI.1–2) and

$$t = \tilde{t}\, t' \qquad \text{(IX.A1)}$$

$$\vec{r} = \tilde{r}\, \vec{r}' \qquad \text{(IX.A2)}$$

$$\tilde{p} = p\, p' \qquad \text{(IX.A3)}$$

with

$$\tilde{t} = (k n_A^{1/3} X_M)^{-1} \tag{IX.A4}$$

$$\tilde{r}^2 = D\,\tilde{t} \tag{IX.A5}$$

$$\tilde{p} = D_f/\kappa_f \tag{IX.A6}$$

$$\kappa^*(\phi) = \kappa(\phi)/\kappa_f, \text{ and } D^*(\phi) = D(\phi)/D_f. \tag{IX.A7}$$

Introducing the new variables t', $\vec{r}'$, and p' into the dynamical equations and then dropping the primes we obtain

$$\frac{\partial(\phi\gamma)}{\partial t} = \vec{\nabla} \cdot [\phi D^*(\phi)\vec{\nabla}\gamma + \phi\gamma\kappa^*(\phi)\vec{\nabla}p] + \frac{1}{\delta}\frac{\partial\phi}{\partial t} \tag{IX.A8}$$

$$\frac{\partial\phi}{\partial t} = (\phi_f - \phi)^{2/3}\ \gamma \tag{IX.A9}$$

$$\vec{\nabla} \cdot [\phi\kappa^*(\phi)\vec{\nabla}p] = (\phi_f - \phi)^{2/3}\,\gamma \tag{IX.A10}$$

The system was taken to be a rectangle as shown in figure 11, where the boundary conditions on the sides of the rectangle are also shown. The domain was divided into a discrete spatial grid, and time was advanced by transforming the partial differential equations for ϕ and γ into a finite (backward) time difference scheme. The p eq (IX.A10) was solved by the "successive over-relaxation" technique (Smith, 1975). For the porosity dependence of the permeability we have chosen the Fair-Hatch

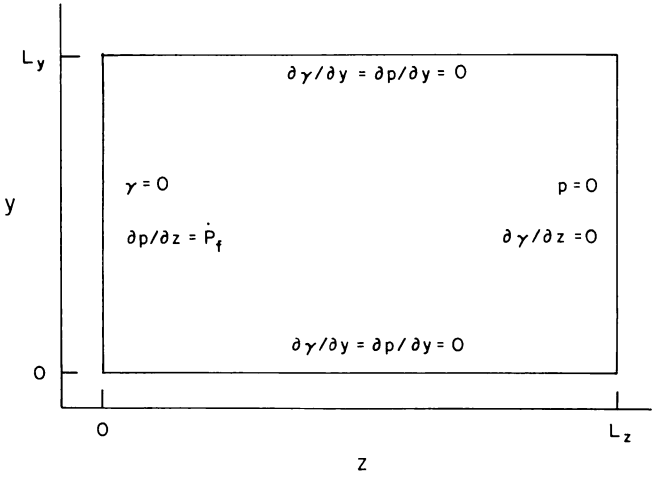

Fig. 11. Shape and boundary conditions of the system for numerical solution of the dynamical equations (sec. IX).

eq (VIII.10), which combined with the definition of $\kappa^*(\phi)$ in (IX.A7) yields

$$\kappa^*(\phi) = \left[\frac{\phi}{\phi_f}\right]^3 \left[\frac{(1 - \phi_f)^{2/3}}{(1 - \phi_f) + \xi(\phi_f - \phi)^{2/3}}\right]^2 \tag{IX.A11}$$

where

$$\xi = (n_A/n_B)^{1/3}. \tag{IX.A12}$$

Also, from the definition in (IX.A7) and taking the effective diffusion coefficient as $D(\phi) = D_o\phi^2$ (Lerman, 1979; D_o is the diffusion coefficient of X in water) we get

$$D^*(\phi) = (\phi/\phi_f)^2. \tag{IX.A13}$$

With these definitions we have the relatively simple formulae

$$\kappa_f^* = D_f^* = 1 \tag{IX.A14}$$

$$\alpha = \frac{v_f}{D_f} = -(\partial p/\partial z)\,|_{z=-\infty} \tag{IX.A15}$$

$$\Gamma = \left[\frac{\phi_0}{\phi_f}\right]^4 \left[\frac{(1 - \phi_f)^{2/3}}{(1 - \phi)^{2/3} + \xi(\phi_f - \phi_0)^{2/3}}\right]^2. \tag{IX.A16}$$

B. Linear Stability Analysis for the Aquifer of Finite Thickness

The linear stability analysis provides useful guidelines for carrying out the numerical simulations. The no-flux boundaries at $y = 0, L_y$ imply

$$\frac{\partial\gamma}{\partial y} = 0 \text{ at } y = 0, L_y. \tag{IX.B1}$$

This no-flux boundary condition implies that m in (VIII.2) can only take the discrete values

$$m = \frac{\pi}{L_y}, \frac{2\pi}{L_y}, \frac{3\pi}{L_y}, \ldots. \tag{XI.B2}$$

The planar dissolution front in the aquifer of finite width ($L_y < \infty$) thus first becomes unstable as m_o of figure 8 reaches the value π/L_y. From (VIII.4) and (VII.3) m_o increases as the water flow velocity increases. Therefore, the critical water flow velocity for which $m_o = \pi/L_y$ is

$$v_{f,c} = \frac{\pi(3 - \Gamma)(1 + \Gamma)}{2L_y(1 - \Gamma)} D_f. \tag{IX.B3}$$

Consequently, the planar reaction front should become unstable for inlet flow velocities greater than the critical value of v_f, that is

$$v_f > v_{f,c}\text{: instability.} \qquad \text{(IX.B4)}$$

It now remains to determine what nonlinear phenomena occur when the critical velocity $v_{f,c}$ is exceeded.

C. Results: Evolution of Porosity Contours

Numerical simulations were carried out to study the transition to instability. The results are presented here as a series of contours of porosity showing the advancement of the dissolution front. Eqs (IX.A8–10,14,16) were simulated at various values of the system parameters. The results are shown in figures 12 to 14; the specific parameter values chosen are given in the captions.

A stable aquifer is shown in figure 12. The porosity contour shown is $(\phi_f + \phi_0)/2$ at various times. The initial state ($\phi(y, z, t = 0)$, $\gamma(y, z, t = 0)$) was taken to be a planar reaction front with a bump near the lower left. As the front advances it becomes planar.

The critical inlet velocity is exceeded in the case of figure 13. The situation is exactly as in figure 12 except for a higher pressure gradient in the altered region and thus a higher inlet flow velocity. Note that now the bump grows to a favored amplitude and shape and then moves downflow with constant velocity and form. The constant shape is to be expected, because as the bump becomes sufficiently long, the X ion brought by the water is consumed laterally, and as a result, in the waters that reach the tip of the finger, the X concentration is sufficiently low to slow down the elongation of the advancing finger. This slowing down counteracts the acceleration produced by the reactive-infiltarion feedback and stabilizes the length-to-width ratio of the finger.

Figure 14 shows a case in which the pressure gradient in the altered region is 10 (five times that in fig. 13). The system is highly unstable. The dissolution finger attains a large amplitude.

X. CONCLUSIONS

The model studies presented demonstrate that scalloping of fluid-rock reaction fronts is an example of geochemical self-organization. The studies suggest that the reactive infiltration feedback mechanism can be present in systems with more complex reaction networks. Because of the generality of the phenomenon we expect that such patterning and flow focusing can be an important aspect of localization and the development of structure in diagenetic and metasomatic systems.

The wavelength and amplitude of scallops depends on the imposed fluid velocity and composition and the mineral content of the unaltered rock. Therefore more detailed geochemical models of these phenomena will provide quantitative constraints on the conditions under which observed scallops developed. In future work we shall develop chemically more realistic models of specific gelogical systems and thereby allow for detailed comparison with field and microscopic study.

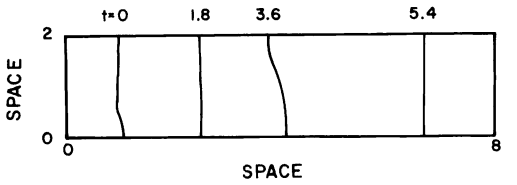

Fig. 12. Time evolution of the midpoint of the reaction front ($(\phi_f + \phi_o)/2$ porosity contour in the ZY plane) obtained as discussed in section IX. Parameter values used in the simulations are $\phi_o = 0.1$, $\phi_f = 0.2$, $X_M = 0.05$, and $(\partial p/\partial z)_f = -0.4$. The overall flow is in the horizontal (Z) direction. Here the initial deviation from the planar profile decays in time; the planar dissolution front is stable.

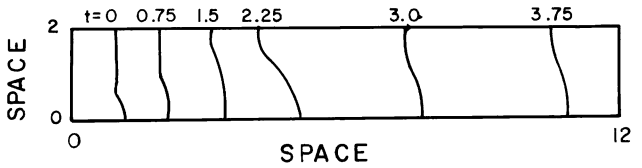

Fig. 13. Same as figure 12 except $(\partial p/\partial z)_f = -2$. Note the bump grows (as predicted by the linear stability analysis) and ultimately reaches a given length.

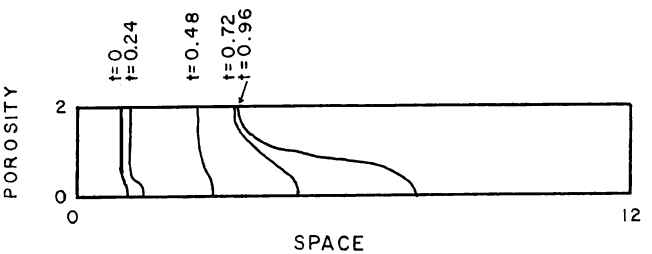

Fig. 14. Same as for figure 12 except that the system is strongly unstable with $(\partial p/\partial z)_f = -10$. Note that the porosity finger becomes extremely elongate.

ACKNOWLEDGMENTS

The authors greatly appreciate the many thoughtful suggestions of the referees.

APPENDIX A

Thickness of the dissolution front

We carry out this calculation ignoring the reactive-infiltration feedback, because we expect this feedback affects only the shape of the front, not its thickness. Thus, the porosity is here taken as uniform and constant. The calculation is carried out in terms of the reaction

$$A_{(s)} \rightleftarrows Y_{(aq)}. \tag{A.1}$$

The front thickness is the distance, along the water flow direction, over which one passes from almost completely dissolved-out A grains upflow to still mostly undissolved ones downflow.

We start out from the continuity equation for the aqueous species Y and the dissolution rate equation for mineral A:

$$\partial Y/\partial t = -\vec{\nabla} \cdot (D\vec{\nabla}Y + \vec{v}Y) - \frac{1}{\phi}\frac{\partial A}{\partial t} \tag{A.2}$$

$$\frac{\partial A}{\partial t} = 3qA^{2/3}(Y - Y^{eq}). \tag{A.3}$$

Here $A = \rho_A n_A L_A^3$ and $3q = n_A^{1/3}\rho_A^{1/3}k\phi$. Changing to the front-fixed reference system as in (V.1),

$$\zeta' = z - ut, \tag{A.4}$$

and denoting $d/d\zeta'$ by a prime ('), (A.2,3) become

$$DY'' + (u - v)Y' + \frac{uA'}{\phi} = 0 \tag{A.5}$$

$$uA' + 3qA^{2/3}(Y - Y^{eq}) = 0. \tag{A.6}$$

The boundary conditions far behind and far ahead of the front are

$$Y(-\infty) = A(-\infty) = 0 \tag{A.7}$$

$$Y(+\infty) = Y^{eq}; \qquad A(+\infty) = A_0. \tag{A.8}$$

We now change (A.5-8) to dimensionless variables γ, a, ζ, η, ν:

$$\begin{aligned} Y &= Y^{eq}\gamma, \quad A = A_0 a \\ \zeta' &= \tilde{\zeta}\zeta, \quad u = \tilde{\zeta}\eta/\tilde{t}, \quad v = \tilde{\zeta}\nu/\tilde{t} \end{aligned} \tag{A.9}$$

with

$$\begin{aligned} \tilde{\zeta}^2 &\equiv D\tilde{t} \\ \tilde{t} &\equiv (qY^{eq}/A_0^{1/3})^{-1} \\ \delta &\equiv \phi Y^{eq}/A_0. \end{aligned} \tag{A.10}$$

With $d/d\zeta$ denoted by a prime, (A.5–8) become

$$\gamma'' + (\mu - \nu)\gamma' + \frac{\mu a'}{\delta} = 0 \tag{A.11}$$

$$\eta a' + 3a^{2/3}(\gamma - 1) + 0 \tag{A.12}$$

$$a(-\infty) = \gamma(-\infty) = 0, \; a(+\infty) = \gamma(+\infty) = 1. \tag{A.13}$$

Eq (A.11) implies that

$$\gamma' + (\eta - \nu)\gamma + \frac{\eta a}{\delta} = \text{constant}.$$

Evaluation of this expression for $\zeta = -\infty$ shows that the constant is zero. Evaluation for $\zeta = +\infty$ yields

$$\eta = \frac{\delta}{1 + \delta}\nu. \tag{A.14}$$

Between (A.14) and the definition

$$a = \lambda^3, \tag{A.15}$$

where λ is the scaledA-grain dimension, (A.11,12) become

$$\gamma' - \frac{\nu}{1+\delta}\gamma + \frac{\nu}{1+\delta}\lambda^3 = 0 \tag{A.16}$$

$$\frac{\delta}{1+\delta}\nu\lambda' = (1-\gamma)H(\lambda), \text{ with } H = \begin{cases} 1, & \lambda > 0 \\ 0, & \lambda \le 0 \end{cases}. \tag{A.17}$$

Near the A dissolution zone we expect that the concentration of Y is near Y^{eq}, that is, γ is near one. We expect the A-dissolution front to be narrow as $\delta \to 0$. To test this hypothesis, we attempt a second scaling of concentration and length according to

$$\gamma = 1 + \delta^{1/2}G \tag{A.18}$$

$$\zeta = \delta^{1/2}r, \tag{A.19}$$

with which (A.16,17) now become as $\delta \to 0$

$$\frac{dG}{dr} + \nu\lambda^3 - \nu = 0 \tag{A.20}$$

$$\nu\frac{d\lambda}{dr} = -GH(\lambda). \tag{A.21}$$

These two equations combine to yield

$$\lambda'' + 1 - \lambda^3 = 0 \tag{A.22}$$

Whatever the exact form of the function $\lambda(r)$, (A.22) shows that λ, the scaled diameter of A-grains, changes on a dimensionless scale of 1.

Characteristic front thickness

The characteristic front thickness Δ equals the product of the two scaling factors introduced for length in (A.9) and (A.19), that is,

$$\Delta = \delta^{1/2}\tilde{\zeta}. \tag{A.23}$$

Using (A.10),

$$\Delta = \delta^{1/2}(DA_o^{1/3}/qY^{eq})^{1/2} \tag{A.24}$$

Finally we evaluate the reaction-rate constant, q, in terms of the lifetime, $t_o(L_{A,o}^3)$, of an equant grain of volume $L_{A,o}^3$ in a fluid with Y held at zero. For such a grain

$$A \equiv L_A^3. \tag{A.25}$$

Then (A.3) becomes

$$\frac{dA}{dt} = -3q(n_A\rho_A)L_A^2Y^{eq}. \tag{A.26}$$

Also, the derivative of A in (A.25) with respect to time is

$$\frac{dA}{dt} = 3n_A\rho_AL_A^2\frac{dL_A}{dt}, \tag{A.27}$$

which, compared to (A.26), yields

$$L_A = L_{A,O} - ft, \text{ with } f = fY^{eq}(n_A\rho_A)^{-1/3}. \tag{A.28}$$

From this, (because at t = tdm R = 0)

$$t_d = L_{A,O}/f \tag{A.29}$$

and

$$k = \frac{A_O^{1/3}}{t_d(L_{A,O}^3)Y^{eq}}. \tag{A.30}$$

Replacing now (A.30) into (A.24) yields

$$\Delta = [\delta D t_d(L_{A,O}^3)]^{1/2} \tag{A.31}$$

which is the desired expression for the front thickness given in (VI.3B).

Appendix B

Kinematics of interface motion

The additional condition (VI.8) needed to determine the reaction-front moving-boundary problem is obtained as follows. Let a point $\vec{r}$ be on the front at time t. Then at a small time ∂t later the point has moved to $\vec{r} \mp u\vec{n}\partial t$, where $\vec{n} = \vec{\nabla}S/|\vec{\nabla}S|$ is the unit normal to the front pointing into the region, and u is the still-to-be-determined normal advancement velocity of the front. Since the new point is also on the front at time $t + \partial t$ we have

$$S(\vec{r} + u\vec{n}\partial t, t + \partial t) = 0. \tag{B.1}$$

Expanding this expression in small ∂t

$$S(\vec{r}, t) + \left(\frac{\partial S}{\partial t} + u\vec{n} \cdot \vec{\nabla}S\right)\partial t + \cdots = 0. \tag{B.2}$$

$S(\vec{r}, t)$ is zero since $\vec{r}$ is on the interface. Thus since ∂t is arbitrary we obtain

$$\frac{\partial S}{\partial t} + u|\vec{\nabla}S| = 0. \tag{B.3}$$

Letting $\tau = \delta t$ and $u = \delta\mu$ we obtain (VI.8).

Appendix C

Pressure gradient jump condition at the dissolution interface

The boundary condition (IV.10) follows from equating the flux of water just upstream of the front to that just downstream from it:

flux just upstream $-\vec{n} \cdot \kappa_f\phi_f\vec{\nabla}p|_{0^+}$;
flux just downstream $-\vec{n} \cdot \phi_f\kappa_f\vec{\nabla}p|_{0^-}$.
$\vec{n}$ is the unit vector normal to the reaction front,
0^- and 0^+ indicate positions just upstream and downstream from the front respectively. Equating the two fluxes yields (IV.10).

Appendix D

Planar front profiles

Solution of the planar front problem (eqs (IV.5, 6) with the boundary conditions (IV.9, 10, 12–14)) proceeds as follows. First, eq (IV.6) implies that the water pressure p must be linear in ζ, both behind and ahead of the front, but with different slopes $p'_f \equiv (dp/d\zeta)_f$ and similarly for p'_0:

$$p = p'_f \zeta \text{ for } \zeta < 0.$$
$$p = p'_o \zeta \text{ for } \zeta > 0. \tag{D.1}$$

The relation between these two fluid pressure gradients behind and ahead of the front is given by condition (VI.10), which implies that

$$p'_f = p'_o \Gamma = p'_o \frac{\phi_o \kappa_o}{\phi_f \kappa_f}. \tag{D.2}$$

Secondly, eq (IV.5) now becomes

$$D_f \gamma'' + \kappa_f p'_f \kappa' = 0 \text{ for } \zeta < 0. \tag{D.3}$$

This has the general solution

$$\gamma = a + be^{\alpha\zeta}, \quad \text{for } \zeta < 0, \tag{D.4}$$

where a and b are constants. From (VI.2), for $\zeta = -\infty$, $\bar{\gamma} = 1$; thus $a = 1$. And from (IV.12), at the front $\zeta = 0$ and $\gamma|_{o+} = 0$, and thus $b = -1$. Therefore (D.4) reduces to

$$\gamma = 1 - e^{\alpha\zeta}, \quad \text{for } \zeta < 0 \tag{D.5}$$

with

$$\alpha = \frac{v_f}{D_f}. \tag{D.6}$$

Appendix E

Details of the morphological stability analysis: derivation of the growth rate of fingers, eq (VIII.3)

It is most convenient to consider the choice $S = z - \bar{\mu}\tau - R(y, \tau)$ in preference to their being viewed as functions of z,y,τ. With this ∇-p = 0 is transformed into

$$\frac{\partial^2 p}{\partial y^2} + \left[1 + \left(\frac{\partial R}{\partial y}\right)^2\right]\frac{\partial^2 p}{\partial S^2} - 2\frac{\partial R}{\partial y}\frac{\partial^2 p}{\partial S \partial y} - \frac{\partial^2 R}{\partial y^2}\frac{\partial p}{\partial S} = 0 \tag{E.1}$$

and similarly for the γ-equation. Although the above equation has a more complex structure the reformulation has the advantage that the γ and p equations now operate on a fixed domain, the moving interface always existing at S = 0.

The boundary conditions may be made more explicit as follows. The normal derivative of p may be written

$$\frac{\partial p}{\partial n} = \frac{\vec{\nabla} \cdot \vec{\nabla} p}{|\vec{\nabla} S|}. \tag{E.2}$$

With this we obtain

$$\frac{\partial p}{\partial n} = \left[1 + \left(\frac{\partial R}{\partial y}\right)^2\right]^{1/2} \frac{\partial p}{\partial S} - \left(\frac{\partial R}{\partial y}\right)\frac{\partial p}{\partial y}. \tag{E.3}$$

A similar result is attained for γ. The dynamics of the interface yields

$$\mu + \frac{\partial R}{\partial \tau} = \mu\left[1 + \left(\frac{\partial R}{\partial y}\right)^2\right]^{1/2} \tag{E.4}$$

The linear stability analysis proceeds by writing

$$\begin{aligned} p &= \bar{p}(S) + \tilde{p} \\ \gamma &= \bar{\gamma}(S) + \tilde{\gamma} \\ R &= \tilde{R} \\ \mu &= \bar{\mu} + \tilde{\mu} \end{aligned} \tag{E.5}$$

Next let $\tilde{R} = \hat{R}e^{\omega\tau}\cos my$, $\tilde{p} = \hat{p}(S)e^{\omega\tau}\cos my$, $\tilde{\mu} = \hat{\mu}e^{\omega\tau}\cos my$, $\tilde{\gamma} = \hat{\gamma}(S)e^{\omega\tau}\cos my$ the interface dynamics read, neglecting quadratic and higher order terms in deviations.

$$\omega\hat{R} = \hat{\mu}. \tag{E.6}$$

Also $\hat{p}$ satisfies

$$\left[\frac{d^2}{dS^2} - m^2\right]\hat{p} + m^2\frac{d\bar{p}}{dS}\hat{R} = 0 \tag{E.7}$$

A similar equation may be obtained for $\hat{\gamma}(S)$.

The $\hat{\gamma}$ and $\hat{p}$ equations are second order and hence yield solutions with two constants in each spatial domain ($S > O$). Since $\gamma = 0$ for $S > 0$ and since $\hat{\gamma}$ and $\hat{p}$ are finite as $|S| \to \infty$, we have three constants from $\hat{\gamma}$ and $\hat{p}$ left to determine. Furthermore ω and $\hat{\mu}$ must be obtained, yielding five unknowns ($\hat{R}$ being fixed by specific initial data). The boundary conditions (VI.10, 12–15) and (E.6) yield five equations to obtain all the unknowns. The results yield (VIII.3) for $\omega(m)$.

References

Bailey, R. V., and Childers, M. D., 1977, Applied mineral exploration with special reference to uranium: Boulder, Colo., Westview Press, 542 p.

Bear, J., 1972, Dynamics of Fluids in Porous Media: Amsterdam, Elsevier, 764 p.

Britten, J. A., and Krantz, W. B., 1984, Linear stability of a planar reverse combustion front propagating through a porous medium: gas-solid combustion model, *in* Nicolis, G., and Baras, F., eds., Chemical Instabilities: NATO Advances Sci Ser. C, v. 120, p. 117–135.

Chadam, J., Hoff, D., Ortoleva, P. and Sen, A., 1986, Reactive-Infiltration Instability: IMA Jour. Appl. Math., 36, p. 207–238.

Chadam, J., and Ortoleva, P., 1986, Moving interfaces and their stability: applications to chemical waves and solidification, *in* Hlavacek, V., ed., Dynamics of Nonlinear Systems: New York, Gordon and Breach Sci. Pub., p. 247–278.

Chandrasekhar, S., 1961, Hydrodynamic and Hydromagnetic Stability: Oxford, Oxford Univ. Press, 652 p.

De Groot, S. R., and Mazur, P., 1962, Nonequilibrium Thermodynamics: Amsterdam, North-Holland, 510 p.

Galloway, W. E., 1978. Uranium mineralization in a coastal-plain fluvial aquifer system: Catahoula Formation, Texas: Econ. Geology, v. 73, p. 1655–1676.

Hill, A. D., ms, 1978, Flow with simultaneous heterogeneous reactions in porous media: Ph.D. thesis, Univ. Texas at Austin, 143 p.

Hutcheon, I., and Oldershaw, A., 1983, Hydrothermal effects on recovery-related properties of carbonate rocks: Internat. Symposium Water-Rock Interaction, 4th, Misasa, Japan, extended Abs., p. 195–197.
Kirkner, D. J., Jennings, A. A., and Theis, T. L., 1985, Multisolute mass transport with chemical interaction kinetics: Jour. Hydrology, v. 76, p. 107–117.
Lerman, A., 1979, Geochemical Processes: New York, Wiley, 481 p.
Merino, E., 1984, Survey of geochemical self-patterning phenomena, *in* Nicolis, G., and Baras, F., eds., Chemical Instabilities: Applications in Chemistry, Engineering, Geology, and Materials Science: NATO Advances Sci. Ser. C, v. 120, p. 305–328.
Nguyen, V. V., Gray, W. G., Pinder, G. F., Botha, J. F., and Crerar, D. A., 1982, A theoretical investigation on the transport of chemicals in reactive porous media: Water Resources Research. v. 18, p. 1149–1156.
Nicolis, G., and Prigogine, I., 1977, Self-Organization in Nonequilibrium Systems: New York, Wiley, 491 p.
Ockendon, J., and Hodgkins, W., 1975, Moving Boundary Problems in Heat Flow and Diffusion: Oxford, Clarendon Press, 300 p.
Ortoleva, P., 1988, Geochemical Self-Organization: Oxford, Oxford Univ. Press, in press.
Ortoleva, P., Merino, E., Moore, C., and Chadam, J., 1987, Geochemical self-organization I: reaction transport feedbacks and modeling approach: Am. Jour. Sci., v. 287, p. 979–1007.
Rubin, J., 1983, Transport of reacting solutes in porous media: relation between mathematical nature of problem formulation and chemical nature of reactions: Water Resources Research, v. 19, p. 1231–1252.
Rubinstein, L., 1971, The Stefan Problem: Providence, R.I., Am. Math. Soc., 419 p.
Schecter, R. S., and Gidley, J. L., 1969, The change in pore size distributions from surface reactions in porous media: Am. Inst. Chem. Eng. Jour., v. 15, p. 339–350.
Schmidt, S., and Ortoleva, P., 1980 Asymptotic solutions of the FKN chemical wave equations: Jour. Chem. Physics, v. 72, p. 2733–2738.
———— 1981, Electrical field effects on propagating BZ waves: predictions of an oregonator and new pulse supporting model: Jour. Chemistry, v. 74, p. 4488–4508.
Sekerka, R. F., 1967, Time dependent theory of stability of a planar interface during dilute binary alloy solidification, *in* Peiser, H. S., ed. Crystal Growth, Oxford, Pergamon, p. 691–702.
Smith, G. D., 1975, Numerical Solutions of Partial Differential Equations: Oxford, Univ. Press, 179 p.